JOURNAL OF GUIDANCE, CONTROL, AND DYNAMICS
Vol. 33, No. 3, May–June 2010

Adaptive Feedforward Control for Gust Load Alleviation

Jie Zeng* and Boris Moulin†
ZONA Technology, Inc., Scottsdale, Arizona 85258
Raymond de Callafon‡
University of California, San Diego, La Jolla, California 92093
and
Martin J. Brenner§
NASA Dryden Flight Research Center, Edwards, California 93523

DOI: 10.2514/1.46091

In this paper, an adaptive feedforward control framework is proposed for the suppression of aircraft structural vibrations induced by gust perturbations to increase the resilience of the flight control law in the presence of the aeroelastic/aeroservoelastic interactions. Currently, aircraft with nonadaptive control laws usually include roll-off or notch filters to avoid aeroelastic/aeroservoelastic interactions. However, if changes in the aircraft configuration are significant, the frequencies of the flexible modes of the aircraft may be shifted, and the notch filters could become totally ineffective. With the proposed approach, the flexible modes can be consistently estimated in real time via a proven system-identification algorithm. The identified flexible modes information is used in the proposed adaptive feedforward control algorithm to adjust the parametrization of the basis functions in a feedforward controller. Along with the recursive least-squares estimate, the feedforward controller is adjusted, and the structural vibration of the aircraft induced by the gust perturbation can be largely suppressed. An F/A-18 active aeroelastic wing aeroelastic model with gust perturbation based on the linear aeroelastic solver formulation is developed as a test bed to demonstrate the proposed adaptive feedforward control algorithm.

Nomenclature

$A(\omega)$	=	denominator matrix polynomial
$B(\omega)$	=	numerator matrix polynomial
$B_i(q)$	=	orthonormal basis function
C	=	damping matrix
$F(q)$	=	feedforward compensator
F_A	=	external aerodynamic forces
F_T	=	thrust forces
F_δ	=	aerodynamic forces from control surfaces
$G(q)$	=	transfer function from control surface to accelerometer sensor
$G(\omega)$	=	frequency response function
$H(q)$	=	transfer function from gust perturbation to accelerometer sensor
K	=	stiffness matrix
$k(t)$	=	gain vector
M	=	mass matrix
M_A	=	external aerodynamic moments
M_T	=	thrust moments
M_δ	=	aerodynamic moments from control surfaces
$P(q)$	=	all pass transfer function
$P(t)$	=	inverse correlation matrix
$Q(s)$	=	aerodynamic force coefficient matrix
q	=	forward shift operator
$[T_A]$	=	transformation matrix
$T_g(s)$	=	Dryden vertical velocity shaping filter
$T_{\mathrm{LPF}}(s)$	=	low-pass filter
$u(t)$	=	control surface command
$w(t)$	=	gust perturbation
x_{Le}	=	aerodynamic lag terms
$y(t)$	=	output signal
β_k	=	coefficients of the orthonormal finite impulse response filter
Δ_F	=	aeroelastic incremental forces
Δ_M	=	aeroelastic incremental moments
η_e	=	generalized coordinate
θ	=	unknown parameters to be estimated
λ	=	forgetting factor
$\phi(t)$	=	regress vector

Subscripts

ee	=	related to the elastic dynamics
i	=	$[r, e, \delta]$ related to the airframe, elastic, control related states
lat	=	related to the lateral dynamics plane
long	=	related to the longitudinal dynamics plane
re	=	related to the coupling between rigid-body dynamics and elastic dynamics
rr	=	related to the rigid-body dynamics

Presented as Paper 6373 at the AIAA Atmospheric Flight Mechanics Conference and Exhibit, Honolulu, HI, 18–21 August 2008; received 22 June 2009; revision received 19 October 2009; accepted for publication 19 October 2009.

*Research and Development Control Systems Engineer; jzeng@zonatech.com. Member AIAA.
†Control Engineer Specialist; boris@zonatech.com. Member AIAA.
‡Associate Professor of Mechanical and Aerospace Engineering; callafon@ucsd.edu.
§Aerospace Engineer; martin.j.brenner@nasa.gov. Senior Member AIAA.

I. Introduction

ACTIVE control techniques for the gust load alleviation/flutter suppression have been investigated extensively in the last few decades to control the aeroelastic response and improve the handling qualities of the aircraft. Nonadaptive feedback control algorithms, such as the classical single input/single output (SISO) techniques [1], the linear quadratic regulator theory [2,3], the eigenspace techniques [4,5], the optimal control algorithm [6], and the H_∞ robust control synthesis technique [7] are efficient methods for the gust load alleviation/flutter suppression. However, because of the time-varying characteristics of the aircraft dynamics due to the varying configurations and operational parameters (such as fuel consumption, air density, velocity and air turbulence), it is difficult to synthesize a

unique control law to work effectively throughout the whole flight envelope. Therefore, a gain scheduling technique is necessary to account for the time-varying aircraft dynamics.

An alternative methodology is the feedforward and/or feedback adaptive control algorithms, by which the control law can be updated at every time step [8–10]. With the novel development of the airborne light detection and ranging (LIDAR) turbulence sensor, available for the accurate measurement of the vertical gust velocity at a considerable distance ahead of the aircraft [11], it becomes feasible to design an adaptive feedforward control to alleviate the structural loads induced by any turbulence and extend the life of the structure. The adaptive feedforward control algorithm developed in [10] showed promising results for vibration suppression of the first wing bending mode. However, an unavoidable constraint for the application of this methodology is the usage of a high order finite impulse response (FIR) filter. As a result, an overwhelming computation effort was needed to suppress the structural vibration of the aircraft.

In this paper, an adaptive feedforward control algorithm, in which the feedforward filter is parameterized using orthonormal basis expansions along with a recursive least-squares (RLS) algorithm with a variable forgetting factor, is proposed for the feedforward compensation of gust loads. With the use of the orthonormal basis expansion, the prior flexible modes information of the aircraft dynamics can be incorporated to build the structure of the feedforward controller. With this strategy, the order of the feedforward filter to be estimated can be largely reduced. As a result, the computation effort is greatly decreased, and the performance of the feedforward controller for gust load alleviation will be enhanced. Furthermore, a fast Fourier transform (FFT)-based Polymax identification method and the stabilization diagram program [12] are proposed to estimate the flexible modes of the aircraft dynamics.

The need for an integrated model of flight dynamics and aeroelasticity is brought about by the emerging design requirements for slender, more flexible, and/or sizable aircraft [such as oblique flying wing, high altitude/long endurance (HALE), Sensorcraft, morphing vehicles, etc.). Furthermore, a desirable unified nonlinear simulator should be formulated in principle by using commonly agreeable terms, from both the flight dynamics and the aeroelasticity fields, in a consistent manner.

A unified integration framework that blends flight dynamics and aeroelastic modeling approaches with wind-tunnel or flight-test-data-derived aerodynamic models has been developed in [13]. This framework considers innovative model updating techniques to upgrade the aerodynamic model with data coming from computational-fluid-dynamics/wind-tunnel tests for a rigid configuration or for data estimated from actual flight tests when flexible configurations are considered.

Closely following the unified integration framework developed in [13], an F/A-18 active aeroelastic wing (AAW) aeroelastic model with gust perturbation is developed in this paper, and this F/A-18 AAW aeroelastic model can be implemented as a test bed for flight control system evaluation and/or feedback/feedforward controller design for gust load alleviation/flutter suppression of the flexible aircraft.

The outline of the paper is as follows. In Sec. II, a feedforward compensation framework is introduced. Section III presents the formulation of the orthonormal finite impulse filter structure. A brief description of a frequency domain Polymax identification method is presented in Sec. IV. In Sec. V, a RLS estimation method with a variable forgetting factor is discussed. Section VI includes the development of a linear F/A-18 AAW aeroelastic model and the application of the adaptive feedforward controller to an F/A-18 AAW aeroelastic model.

II. Analysis of the Feedforward Controller

To analyze the design of the feedforward controller F, consider the simplified block diagram of the structural vibration control of the SISO dynamic system depicted in Fig. 1. The gust perturbation $w(t)$ passes through the primary path H, the body of the aircraft, to cause the structural vibrations. Mathematically, H can be characterized as

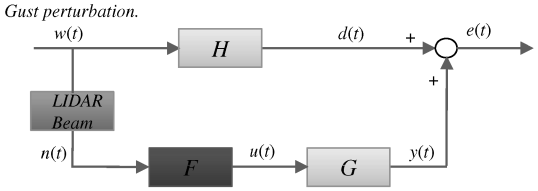

Fig. 1 Block diagram of the structural vibration control with feedforward compensation.

the model/transfer function from the gust perturbation to the accelerometer sensor position. The gust perturbation $w(t)$ can be measured by the coherent LIDAR beam airborne wind sensor. The measured signal $n(t)$ is fed into the feedforward controller F to calculate the control surface demand $u(t)$ for vibration compensations. The structural vibrations are measured by the accelerometers providing the error signal $e(t)$. G is the model/transfer function from the corresponding control surface to the accelerometer sensor position, which is the so-called secondary path.

To apply the feedforward control algorithm for gust loads alleviation, developing a proper sensor to accurately measure the gust perturbation is crucial for the success of the feedforward control application. As mentioned in [11], such a sensor should meet the following criteria:

1) The sensor has the capability to take a feedforward-looking measurement of 50 to 150 m to ensure that the measured air flow is the one actually affecting the aerodynamics around the aircraft.

2) The sensor must be able to measure the vertical wind speed.

3) The standard deviation of the wind-speed measurement should be small, at least in the range of [2–4] m/s.

4) The sensor must be able to produce reliable signals in the absence of aerosols.

5) The sensor must have a good longitudinal resolution (the thickness of the air slice measured ahead).

6) The sensor must have a good temporal resolution.

A sensor system that meets these requirements is a so-called short-pulse UV Doppler LIDAR and was developed in [11]. This short pulse UV Doppler LIDAR was successfully applied to an Airbus 340 to measure the vertical gust speed [14]. The authors in [14] claimed that the system was ready to be used to design feedforward control for gust load alleviation.

Assuming a perfect gust perturbation signal can be measured via the LIDAR beam sensor means $n(t) = w(t)$ and the error signal $e(t)$ can be described by

$$e(t) = [H(q) + G(q)F(q)]w(t) \tag{1}$$

In case the transfer functions in Eq. (1) are known, an ideal feedforward controller $F(q) = F_i(q)$ can be obtained by

$$F_i(q) = -\frac{H(q)}{G(q)} \tag{2}$$

in case $F_i(q)$ is a stable and causal transfer function. The solution of $F_i(q)$ in Eq. (2) assumes full knowledge of $G(q)$ and $H(q)$. Moreover, the filter $F_i(q)$ may not be a causal or stable filter, due to the dynamics of $G(q)$ and $H(q)$, which dictates the solution of the feedforward controller $F_i(q)$. An approximation of the feedforward filter $F_i(q)$ can be made by an output-error-based optimization that aims at finding the best causal and stable approximation $F(q)$ of the ideal feedforward controller in $F_i(q)$, in Eq. (2).

A direct adaptation of the feedforward controller $F(q, \theta)$ can be performed by considering the parameterized error signal $e(t, \theta)$:

$$e(t, \theta) = H(q)w(t) + F(q, \theta)G(q)w(t) \tag{3}$$

Defining the signals

$$d(t) := H(q)w(t), \qquad u_f(t) := -G(q)w(t) \tag{4}$$

where $d(t)$ can actually be measured and $u_f(t)$ is the called filtered input signal, Eq. (3) is reduced to

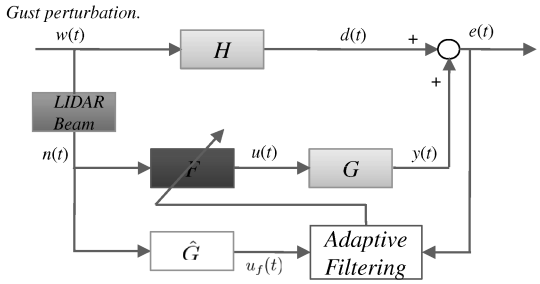

Fig. 2 Block diagram of the structural vibration control with adaptive feedforward compensation.

$$e(t,\ \theta) = d(t) - F(q,\ \theta)u_f(t) \tag{5}$$

for which the minimization

$$\min_{\theta} \frac{1}{N}\sum_{t=1}^{N} e^2(t,\ \theta) \tag{6}$$

to compute the optimal feedforward filter $F(q,\ \theta)$ is a standard output error (OE) minimization problem in a prediction error framework [15].

The minimization of Eq. (6) for $\lim_{N\to\infty}$ can be rewritten into the frequency domain expression:

$$\min_{\theta} \int_{\pi}^{-\pi} |H(e^{jw}) + G(e^{jw})F(e^{jw},\ \theta)|^2 \tag{7}$$

using Parceval's theorem [15]. It can be observed that the standard OE minimization problem in Eq. (6) can be used to compute the optimal feedforward filter $F(q,\ \theta)$, provided $d(t)$ and $u_f(t)$ in Eq. (4) are available.

For a proper derivation of the adaptation of the feedforward filter F, an approximate model $\hat{G}$ of the secondary path G is required to create the filtered signal $u_f(t)$ for the adaptive filtering purpose. The adaptation of the feedforward filter is illustrated in Fig. 2. The filtered signal $u_f(t)$ and the error signal $e(t)$ are used for the computation of the coefficients of the feedforward filter by the adaptive filtering. Thus, the coefficients of the feedforward filter F can be updated at each time constant for structural vibration reduction. Note that the algorithm presented in Fig. 2 only works if G is scalar, as GF is replaced by FG.

III. Orthonormal Finite Impulse Response Filter Structure

In general, the feedforward filter F in Fig. 1 can be realized by adopting both the FIR structure as well as the infinite impulse response (IIR) structure. Because the FIR filter incorporates only zeros, it is always stable and will provide a linear phase response. It is the most popular adaptive filter, widely used in adaptive filtering. Generally, the discrete time linear time invariant FIR filter $F(q)$ can be presented as

$$F(q) = \sum_{k=0}^{L-1} \beta_k q^{-k} \tag{8}$$

where q^{-1} denotes the usual time shift operator, $q^{-1}x(t) = x(t-1)$. Adaptive filter estimation using FIR filters converges to optimal and unbiased estimates, irrespective of the coloring of the noise on the output data. However, a FIR filter is usually too simple to model complex system dynamics, such as aeroelastic/aeroservoelastic systems with many resonance modes being excited by atmospheric perturbations. As a result, many tapped delay coefficients of the FIR filter are required to approximate the optimal filter. Even though an IIR filter is appealing as an alternative, the inherent stability and bias estimation problems limit the use of an IIR filter for adaptive filtering in aeroservoelastic systems.

To improve the approximation properties of the adaptive filter F in Fig. 1, the linear combination of the tapped delay functions q^{-1} in the FIR filter of Eq. (8) can be generalized to the following form:

$$F(q,\ \theta) = \sum_{k=0}^{L-1} \beta_k B_k(q) \tag{9}$$

where $B_k(q)$ are generalized (orthonormal) basis functions [16] that contain some a priori knowledge on the desired filter dynamics. In other words, the orthonormal basis functions that are used in the parametrization of the orthonormal finite impulse response (ORTFIR) filter will be tuned on the fly by taking full advantage of the modal information embedded in the flight data.

A. Construction of the Orthonormal Basis Sets

The application of orthonormal basis functions to parameterize and estimate dynamical systems has obtained extensive attention in recent years. Different constructions of the orthonormal basis structure have been reported in [16–18]. It is assumed that the pole locations are already known with the use of the standard open-loop prediction error system identification methods. Suppose the poles $\{\xi_i\}_{i=1,\,2,\,\cdots,\,N}$ are known; an all pass function $P(q)$ can be created by these poles and is given as

$$P(q) = \prod_{i=1}^{N}\left[\frac{1-\xi_i^* q}{q-\xi_i}\right] \tag{10}$$

Let $(A,\ B,\ C,\ D)$ be a minimal balanced realization of an all pass function $P(q)$ and define the input-to-state transfer function $B_0(q) = (qI - A)^{-1}B$; then, a set of functions $B_i(q)$ can be obtained via

$$B_i(q) = B_0(q)P^i(q) \tag{11}$$

and $B_i(q)$ has orthogonal property:

$$\frac{1}{2\pi j}\oint B_i(q)B_k^T(1/q)\frac{\mathrm{d}q}{q} = \begin{cases} I & i = k \\ 0 & i \neq k \end{cases} \tag{12}$$

The construction of the orthonormal basis function is illustrated in Fig. 3. It should be noted that if $B_0(q)$ includes all the information of a dynamical system, then only one parameter β_0 needs to be estimated to approximate this dynamic system. It means that the parameters estimated will directly depend on the a priori system information injected into the basis functions $B_i(q)$.

An important property and advantage of the ORTFIR filter is that the knowledge of the (desired) dynamical behavior can be incorporated throughout the basis functions $B_i(q)$. As a result, an accurate description of the filter to be estimated can be achieved by a relatively small number of coefficients.

B. Illustration of the Orthonormal Finite Impulse Filter

A 4-degrees-of-freedom (DOF) lumped parameter system is considered to demonstrate the advantage of using the ORTFIR filter over the FIR filter. An illustration of this 4-DOF lumped parameter system is shown in Fig. 4, where k_i and $c_i (i = 1,\ \cdots,\ 5)$ indicate the

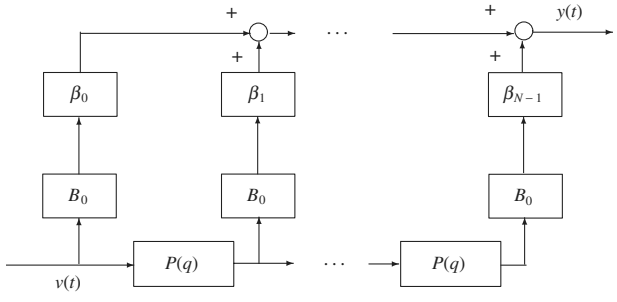

Fig. 3 ORTFIR filter topology.

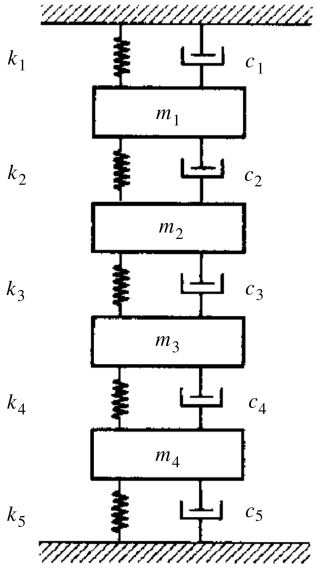

Fig. 4 Lumped parameter system.

system stiffness and damping, respectively, and $m_i (i = 1, \cdots, 4)$ are the masses. The nominal values of these parameters are given as

$$m_1 = m_2 = m_3 = m_4 = 1, \qquad k_1 = k_3 = k_5 = 1750$$
$$k_2 = k_4 = 2000, \qquad c_1 = c_3 = c_5 = 0.7, \qquad c_2 = c_4 = 0.8 \quad (13)$$

A mathematical model of this lumped system can be easily derived with the use of Newton's second law. The natural frequencies and damping ratios of this lumped system are also obtained. For simplicity purposes, all the units of this 4-DOF lumped system are omitted. This mathematical model is applied in this case example as the real model; an FIR model and ORTFIR model will be implemented to approximate this real model, respectively. To facilitate the model estimation using the input and output data of the 4-DOF lumped parameter system, a band-limited white noise (zero mean) is injected into the 4-DOF lumped xparameter system, and an additional band-limited white noise (zero mean) is added to the output response to simulate the measurement noise. With the collected input/output data, an FIR filter with varying order is applied to fit the real model and the variance of the simulation error (the difference of the measured and the simulated output) is used to indicate the performance of the FIR filter.

Furthermore, the Polymax identification method, described in Sec. IV, is applied in this case example to estimate the four physical modes. These estimated modes (shown in Sec. IV using the Polymax method) are used for the basis function generation of the ORTFIR filter. Finally, an eight-order ORTFIR filter is applied to approximate the physical system. The estimation results are shown in Table 1. From Table 1, it is clearly seen that with the FIR filter, the optimal FIR filter will be of the 400th order, with the smallest simulation error at 36.18. However, with the simplest eight-order ORTFIR filter, the variance of the simulation error is only 13.18, which is almost three times smaller than that of the 400th order of the FIR filter. Figure 5 compares the model estimation results using the 50th/200th-order FIR filters and the 8th-order ORTFIR filter. From Fig. 5, it is observed that, with the 50th-order FIR filter, the essential dynamics of the physical system can hardly be approximated. With the 200th-order FIR filter, even though the physical system can be correctly approximated, the estimated model has evident variation (especially in the high frequency range). On the other hand, with 8th-order ORTFIR filter, the physical system can be perfectly approximated; no visible variation of the estimated model was found in a wider frequency range.

Table 2 Comparison between the identified modes and the real modes

Number of modes	Real modes	Identified modes
f_1, Hz	4.1866	4.1868
f_2, Hz	7.8648	7.8630
f_3, Hz	11.3191	11.3303
f_4, Hz	13.1320	13.1320
ζ_1, %	0.5261	0.5622
ζ_2, %	0.9883	1.1035
ζ_3, %	1.4224	1.4836
ζ_4, %	1.6502	1.6333

IV. Modal Parameter Estimation Frequency Polymax Identification

A rather general frequency domain identification method, using the standard least-squares estimator algorithm, is introduced and applied to extract the modal characteristics of a dynamic system from a set of measured data. Consider a set of noisy complex frequency response function (FRF) measurement data, $G(\omega_j)$ $(j = 1, \cdots, N)$. The approximation of the data by a model $P(\omega)$ is addressed by considering the following additive error:

$$E(\omega_j) = G(\omega_j) - P(\omega_j), \qquad j = 1, \cdots, N \quad (14)$$

Then, it is assumed that the model $P(\omega)$ can be represented by a right polynomial fraction matrix given by

$$P(\omega) = [B(\omega)][A(\omega)]^{-1} \quad (15)$$

where $P(\omega) \in \mathcal{C}^{p\times m}$ is the FRF matrix with p outputs and m inputs, $B(\omega) \in \mathcal{C}^{p\times m}$ is the numerator matrix polynomial, and $A(\omega) \in \mathcal{C}^{m\times m}$ is the denominator matrix polynomial.

The matrix polynomial $B(\omega)$ is parameterized by

$$B(\omega) = \sum_{k=0}^{n_b} B_k \xi_k(\omega) \quad (16)$$

where $B_k \in \mathcal{R}^{p\times m}$, and n_b is the number of nonzero matrix coefficients in $B(\omega)$, or the order of $B(\omega)$. The polynomial basis functions are $\xi_k(\omega)$. For the continuous time model, $\xi_k(\omega) = -i\omega_k$. For the discrete time model, $\xi_k(\omega) = e^{-i\omega_k T}$ (T is the sampling time).

The matrix polynomial $A(\omega)$ is parameterized by

$$A(\omega) = \sum_{k=0}^{n_a} A_k \xi_k(\omega) \quad (17)$$

where $A_k \in \mathcal{R}^{m\times m}$, and n_a is the number of nonzero matrix coefficients in $A(\omega)$.

Assuming that the coefficients of the denominator $A(\omega)$ are $[A_0, A_1, \cdots, A_{n_a}]$, a constraint of $A_0 = I_m$ is set to obtain a stable model to fit the measured frequency domain data. Here, a constraint of $A_{n_a} = I_m$ is adopted to extract physical modes from the measured frequency domain data [19].

With $A_{n_a} = I_m$, the poles of the estimated model are separated into stable physical poles and unstable mathematical poles, from which a very clean stabilization diagram can be obtained, and the physical

Table 1 Model estimation results using FIR filter and the ORTFIR filter

Order	1000	500	400	300	200	100	50	8
Filter type	FIR	FIR	FIR	FIR	FIR	FIR	FIR	ORTFIR
Variance of simulation error	42.53	36.46	36.18	36.70	40.28	52.91	70.10	13.18

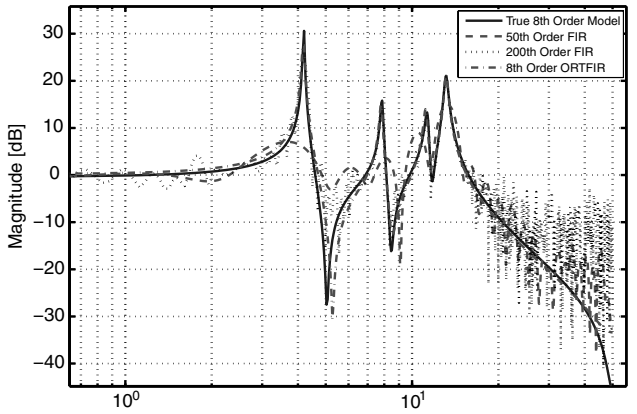

Fig. 5 Comparison of the model estimation using the FIR and ORTFIR filters.

modal parameters of the real system can be estimated from a quick evaluation of the generated stabilization diagram [20].

The stabilization diagram assumes an increasing model order (number of poles noted in the left ordinate axis), and it indicates where the poles are located on the frequency axis. As a rule, unstable poles are not considered in the plot. Physical poles will appear as stable poles, independent of the number of the assumed model order. On the other hand, mathematical poles that intend to model the noise embedded in the data, will change with the assumed model order.

As an example, the 4-DOF lumped system used in Sec. III is applied in this section to demonstrate the Polymax identification method. Figure 6a depicts the stabilization diagram for the 4-DOF lumped system, in which four physical modes can be easily appreciated with the parameter constraint of $A_{n_a} = I_1$. The estimation results can be easily extracted through the access of the stabilization diagram, and they are shown in Table 2. However, within $A_{n_0} = I_1$, the physical modes are difficult to extract from the stabilization diagram, because with this parameter constraint, all the mathematical poles are also estimated as the stable poles. This phenomenon is illustrated in Fig. 6b. In Figs. 6a and 6b, the solid curve indicates the FRF estimate from the input and output time domain data, and the dotted curve indicates the estimated model with the highest order of 50. The right ordinate axis is the magnitude in dB, which is used to present (in frequency domain) the magnitude of the FRF and the estimated 50th-order model. The markers indicate different damping values of each estimated stable pole displayed in the stabilization diagram. The detailed meanings of these damping markers are presented in Table 3.

In Table 2, the second column indicates the frequency and damping of the true modes. The third column presents the estimated frequency and damping of the true modes, using the proposed Polymax identification method and stabilization diagram. Comparing the

Table 3 Damping markers in the stabilization diagram

Range of damping ratio	Marker sign
$0 < \zeta < 0.1\%$	+
$0.1\% < \zeta < 1\%$	×
$1\% < \zeta < 2\%$	*
$2\% < \zeta < 4\%$	◆
$4\% < \zeta < 6\%$	▽
$6\% < \zeta$	△

estimated modes and real modes (calculated from the mathematical equation of motion of the 4-DOF lumped system) in Table 2, it is obvious that the frequency f_i and the damping, $\zeta_i (i = 1, 2, 3, 4)$ of these four physical modes are estimated consistently.

V. Recursive Least-Squares Adaptive Algorithm

The adaptive algorithm to be implemented is the RLS algorithm [21]. Given the input and output data, it can be written in regressor form:

$$y(t) = \phi^T(t)\theta + e(t), \qquad \theta = [\beta_0, \beta_1, \ldots, \beta_{L-1}]^T \tag{18}$$

where $\phi^T(t) = [u_0^T(t), \ldots, u_{L-1}^T(t)]$ is the available input data vector, θ is the parameter vector to be estimated of the ORTFIR feedforward controller, and $e(t)$ is the residue error. The parameters θ can be identified with the available input-output data up to time t by a standard RLS algorithm. It is well known that the RLS algorithm at the steady-state operation exhibits a windup problem if the forgetting factor remains constant, which will deteriorate the estimation results. As a result, a variable forgetting factor [22] is sought to prevent this problem from occurring. The parameters θ can be estimated by the RLS algorithm using a variable forgetting factor through a two-step approach at each sample time:

1. Compute the gain vector $k(t)$ and the parameters $\hat{\theta}(t)$ at the current sample time as

$$\hat{\theta}(t) = \hat{\theta}(t-1) + k(t)\xi^T(t) \tag{19}$$

$$\xi(t) = y(t) - \hat{\theta}^T(t-1)\phi(t) \tag{20}$$

$$k(t) = \frac{P(t-1)\phi(t)}{\lambda_1(t) + \phi^T(t)P(t-1)\phi(t)} \tag{21}$$

2. Update the inverse correlation matrix $P(t)$ and the forgetting factor $\lambda(t)$:

$$P(t) = \lambda(t)^{-1}[1 - k(t)\phi^T(t)]P(t-1) \tag{22}$$

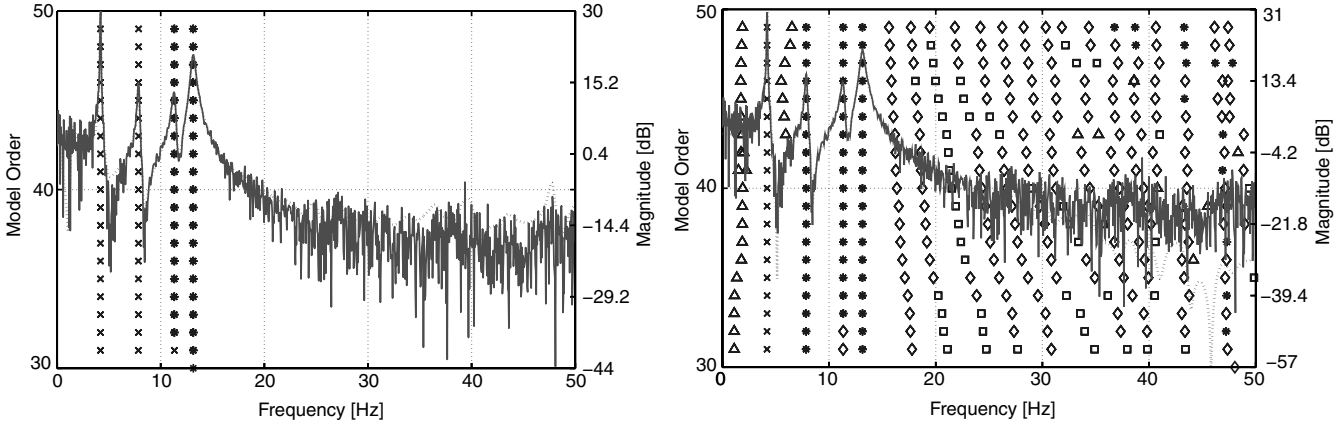

a) Stabilization Diagram with $A_{n_a} = I_1$

b) Stabilization Diagram with $A_{n_0} = I_1$

Fig. 6 Illustration of the stabilization diagram using the Polymax identification method.

$$\lambda(t) = \lambda_{\min} + (1 - \lambda_{\min}) \cdot 2^{-L(t)}, \qquad L(t) = \text{round}(\rho \cdot \xi(t)^2) \quad (23)$$

where ρ is a design parameter that controls the change rate and the width of a unity zone, and $\xi(t)$ is the estimation error, which is calculated via Eq. (20). The lower bound of λ is defined by $\lambda_{\min}$.

In Eq. (23), it is shown that when the estimation error $e(t)$ and $L(t)$ are small, $2^{-L(t)} \to 1$ and $\lambda(t) \to 1$ at an exponential rate, and this rate is controlled by ρ. When $\xi(t)$ increases to infinity, λ reaches its minimum value. The RLS minimization is posted as

$$J(t) = \sum_{i=1}^{t} \lambda(i)^{t-i} [y(i) - \hat{\theta}(t)^T \phi(i)]^2 \quad (24)$$

By choosing the variable forgetting factor, indicated in Eq. (23), the fast decrease of the inverse correlation matrix $P(t)$ can be avoided at the beginning of the estimation. In general, this will result in an accelerated convergence by maintaining a high adaptation at the beginning of the estimation when the parameters θ are still far from the optimal value.

VI. Application to the Closed-Loop F/A-18 Active Aeroelastic Wing Linear Model

A. Linear Aeroelastic Solver Formulation Approach

A unified aeroelastic formulation to take into account the influence of aeroelastic effects on the flight dynamic behavior of the whole aircraft has been developed in [23].

A general formulation of a flexible aircraft with respect to a body-fixed reference system driven by aerodynamic, thrust, and gravity (g) forces and moments can be defined as

$$m\{\dot{V}_b + \Omega_b \times V_b - R_{bg}(E)[0, 0, g]^T\} = F_A + F_\delta + F_T + \Delta_F$$
$$J\dot{\Omega}_b + \Omega_b \times J\Omega_b = M_A + M_\delta + M_T + \Delta_M \quad (25)$$

where, m and J are the air vehicle mass and inertia tensor, and $R_{bg}(E)$ is the rotation mapping from the inertial to body axes ($E = [\phi,\ \theta,\ \psi]$).

Equation (25) is driven by the forces and moments on its right-hand side, where F_A and M_A are the external aerodynamic forces and moments on the air vehicle. F_A and M_A are a function of the aerodynamic flight states ($V, \alpha, \beta, E, \ldots$, etc.), Mach number, body angular rates (Ω_b), and control surface deflections and are usually obtained by wind-tunnel or flight tests. In either case, the quasi-steady influence of the deformed air vehicle is included by considering flexible-to-rigid ratios or parameter identification (PID) techniques, [24,25]. F_δ and M_δ are the aerodynamic forces and moments from the control surfaces commanded by the flight control system and pilot inputs, whereas F_T and M_T include the thrust loads.

In addition, Δ_F and Δ_M are the aeroelastic incremental loads due to the structural deformation. Usually, these loads are assumed to be quasi statics and can be computed by a static aeroelastic analysis. However, this quasi-static assumption may not be sufficient for a highly reconfigurable and flexible aircraft like the new generation of morphing unmanned aerial vehicle, HALEs, etc., for which the interaction between the dynamic structural deformation due to unsteady flow and rigid-body motion can play an important role.

During the integration process, the aeroelastic equations of motion (EOM) underwent two similarity transformation steps, and so the generalized coordinates related with the six rigid-body modes originally defined in the principle axes are mapped into the airframe states (stability axes definition). Specifically, for symmetric maneuvers, the transformation matrix $[T_A]_{\text{long}}$ [23] reads as

$$\begin{Bmatrix} T_x \\ T_z \\ R_y \\ \dot{T}_x \\ \dot{T}_z \\ \dot{R}_y \end{Bmatrix} = \underbrace{\begin{bmatrix} -1 & 0 & 0 & 0 & 0 & 0 \\ 0 & 0 & 1 & 0 & 0 & 0 \\ 0 & 0 & 0 & 0 & 1 & 0 \\ 0 & -1 & 0 & 0 & 0 & 0 \\ 0 & 0 & 0 & -V & V & 0 \\ 0 & 0 & 0 & 0 & 0 & 1 \end{bmatrix}}_{[T_A]_{\text{long}}} \begin{Bmatrix} x \\ u \\ h \\ \alpha \\ \theta \\ q \end{Bmatrix} \quad (26)$$

For an antisymmetric maneuver, $[T_A]_{\text{lat}}$ is

$$\begin{Bmatrix} T_y \\ R_x \\ R_z \\ \dot{T}_y \\ \dot{R}_x \\ \dot{R}_z \end{Bmatrix} = \underbrace{\begin{bmatrix} 1 & 0 & 0 & 0 & 0 & 0 \\ 0 & 0 & 0 & 0 & -1 & 0 \\ 0 & 0 & 0 & 0 & 0 & -1 \\ 0 & V & 0 & 0 & 0 & V \\ 0 & 0 & -1 & 0 & 0 & 0 \\ 0 & 0 & 0 & -1 & 0 & 0 \end{bmatrix}}_{[T_A]_{\text{lat}}} \begin{Bmatrix} y \\ \beta \\ p \\ r \\ \phi \\ \psi \end{Bmatrix} \quad (27)$$

For an asymmetric maneuver, the matrix $[T_A] \in \mathbf{R}^{12\times 12}$ will be composed by the proper allocation of the elements that form the rows and columns of the $[T_A]_{\text{long}}$ and $[T_A]_{\text{lat}}$ matrices.

In this new coordinate system, the linear aeroelastic EOM are

$$\left\{ \begin{bmatrix} M_{rr} & 0 \\ 0 & M_{ee} \end{bmatrix} s^2 + \begin{bmatrix} C_{rr} & 0 \\ 0 & C_{ee} \end{bmatrix} s + \begin{bmatrix} K_{rr} & 0 \\ 0 & K_{ee} \end{bmatrix} \right\} \begin{Bmatrix} \xi_{as} \\ \eta_e \end{Bmatrix}$$
$$= q_\infty \left\{ \begin{bmatrix} Q_{rr}(s) & Q_{re}(s) \\ Q_{er}(s) & Q_{ee}(s) \end{bmatrix} \begin{Bmatrix} \xi_{as} \\ \eta_e \end{Bmatrix} + \begin{bmatrix} Q_{r\delta}(s) \\ Q_{e\delta}(s) \end{bmatrix} \delta_u + \begin{bmatrix} \frac{1}{V} & Q_{rG}(s) \\ & Q_{eG}(s) \end{bmatrix} w_G \right\} \quad (28)$$

where w_G is the gust input; the elastic generalized coordinates η_e, the input, and the δ_u vectors are

$$\eta_e^T = [\,\eta_{e_1},\ \ldots,\ \eta_{e_{N_e}}\,]^T, \qquad \delta_u^T = [\,\delta_{\text{elev}},\ \delta_{\text{ail}},\ \delta_{\text{rud}},\ \ldots\,]^T$$

It should be noted that the equations are only coupled via external forces and moments. In addition, after the transformation is applied to the generalized mass matrix of the finite element model, it is no longer necessarily diagonal. In fact, the submatrix M_{rr} associated with the rigid-body modes is identical to the mass matrix in the flight dynamics equation (i.e., the offdiagonal terms contain the products of inertia):

$$M_{rr} = \text{diag}(mI_3,\ J) \quad (29)$$

Usually, the aerodynamic force coefficient matrix $Q(s)$ is approximated using the rational function approximation (RFA) approach as

$$Q(s) = [A_0] + [A_1]\frac{L}{V}s + [A_2]\frac{L^2}{V^2}s^2 + [D]\left(sI - \frac{V}{L}[R]\right)^{-1}[E]s \quad (30)$$

where the $[A_i]$ ($i = 0,\ 1,\ 2$), $[D]$, and $[E]$ matrices are column partitioned as

$$[A_i] = [\,A_r \quad A_e \quad A_\delta\,] \quad (31)$$

where $i = r, e, \delta$ are the airframe-, elastic-, and control-related states.

In this formulation, the $[A_i]$ coefficient matrices represent the quasi-steady aerodynamic forces, and the remnant terms are used to model the flow unsteadiness by the Padé approximation.

Using the minimum state approach during the RFA implemented in the ZAERO/ASE module [26], and due to the performed similarity transformation, the aerolag terms are computed as

$$\{\dot{x}_L\} = \frac{V}{L}[R]\{x_L\} + [\,E_{L*} \quad E_{Lr} \quad E_{Le} \quad E_{L\delta}\,] \begin{Bmatrix} \xi_{as} \\ \dot{\xi}_{as} \\ \dot{\eta}_e \\ \delta_u \end{Bmatrix} \quad (32)$$

$$z_L = [\,D\,]\{\,x_L\,\} \quad (33)$$

By including Eqs. (30) and (32) into Eq. (28), the aeroelastic EOM can now be easily partitioned in accordance with the airframe DOF,

elastic dynamics, aerodynamic lag terms, a set of control inputs, and gust perturbation as

$$\begin{Bmatrix} \dot{\xi}_{as} \\ \ddot{\xi}_{as} \\ \dot{\eta}_e \\ \ddot{\eta}_e \\ \dot{x}_L \end{Bmatrix} = \begin{bmatrix} A_{\xi_{as}} & A_{\dot{\xi}_{as}} & 0 & 0 & 0 \\ A_{rr_0} & A_{rr_1} & A_{re_0} & A_{re_1} & A_{rL} \\ 0 & 0 & 0 & I & 0 \\ A_{er_0} & A_{er_1} & A_{ee_0} & A_{ee_1} & A_{eL} \\ E_{L*} & E_{Lr} & 0 & E_{Le} & \frac{V}{L}R \end{bmatrix} \begin{Bmatrix} \xi_{as} \\ \dot{\xi}_{as} \\ \eta_e \\ \dot{\eta}_e \\ x_L \end{Bmatrix} + \begin{bmatrix} 0 & 0 & 0 \\ B_{r_0} & B_{r_1} & B_{r_2} \\ 0 & 0 & 0 \\ B_{e_0} & B_{e_1} & B_{e_2} \\ 0 & E_{L\delta} & 0 \end{bmatrix} \begin{Bmatrix} \delta_u \\ \delta_{\dot{u}} \\ \delta_{\ddot{u}} \end{Bmatrix} + \begin{bmatrix} 0 & 0 \\ B_{r_{w1}} & B_{r_{w2}} \\ 0 & 0 \\ B_{e_{w1}} & B_{e_{w2}} \\ 0 & E_{rG} \end{bmatrix} \begin{Bmatrix} w_G \\ \dot{w}_G \end{Bmatrix} \quad (34)$$

where $A_{\xi_{as}}$, $A_{\dot{\xi}_{as}}$, and E_{L*} are coupling matrices due to the similarity transformation executed. Now, the aeroelastic incremental loads Δ_F and Δ_M should be implemented in a way to allow a seamless integration between the nonlinear flight dynamics and the linear aeroelastic EOM. In fact, this can be easily achieved in accordance with the partitions [shown in Eq. (34)] between the rigid, elastic, and aerodynamic lag dynamics. Hence, the aeroelastic incremental loads are computed similarly to the approximation given by Eq. (30):

$$\begin{bmatrix} \Delta_F \\ \Delta_M \end{bmatrix} = q_\infty \left\{ A_{0_{re}} \bar{\eta}_e + A_{1_{re}} \frac{L}{V} \dot{\eta}_e + A_{2_{re}} \frac{L^2}{V^2} \ddot{\eta}_e + D_{re} x_{Le} \right\} \quad (35)$$

Clearly, to implement this algebraic equation, the generalized coordinate $\bar{\eta}_e = \eta_e - \eta_{e_0}$, its rate $\dot{\eta}_e$, its acceleration $\ddot{\eta}_e$, and its vectors, as well as the aerodynamic lag terms related with the elastic modes x_{L_e}, must be estimated at each time iteration.

Decoupling the airframe state ξ_{as} and the aeroelastic state η_e requires the decoupling of the aerolag states x_L from the airframe state ξ_{as} and the aeroelastic state η_e. According to Eq. (32), the following augmented equation is devised to decouple the generalized coordinate's aerolag terms:

$$\begin{Bmatrix} \dot{x}_{L_{as}} \\ \dot{x}_{L_e} \end{Bmatrix} = \begin{bmatrix} \frac{V}{L}R & 0 \\ 0 & \frac{V}{L}R \end{bmatrix} \begin{Bmatrix} x_{L_{as}} \\ x_{L_e} \end{Bmatrix} + \begin{bmatrix} E_{L*} & E_{Lr} & 0 & E_{Le} \\ 0 & 0 & 0 & E_{Le} \end{bmatrix} \begin{Bmatrix} \xi_{as} \\ \dot{\xi}_{as} \\ \eta_e \\ \dot{\eta}_e \end{Bmatrix} + \begin{bmatrix} 0 & 0.5E_{L\delta} & 0 \\ 0 & 0.5E_{L\delta} & 0 \end{bmatrix} \begin{Bmatrix} \delta_u \\ \delta_{\dot{u}} \\ \delta_{\ddot{u}} \end{Bmatrix} + \begin{bmatrix} 0 & 0.5E_{rG} \\ 0 & 0.5E_{rG} \end{bmatrix} \begin{Bmatrix} w_G \\ \dot{w}_G \end{Bmatrix} \quad (36)$$

$$\begin{Bmatrix} z_{L_{as}} \\ z_{L_e} \end{Bmatrix} = [D \quad D] \begin{Bmatrix} x_{L_{as}} \\ x_{L_e} \end{Bmatrix} \quad (37)$$

In this way, only elastic lag terms are considered to avoid any possible coupling with the rigid-body airframe related states (i.e., ξ_{as} and $\dot{\xi}_{as}$). Now, the following differential equation is obtained, combining the lower partition of Eq. (34) with the newly devised Eq. (36):

$$\underbrace{\begin{Bmatrix} \dot{\eta}_e \\ \ddot{\eta}_e \\ \dot{x}_{L_{as}} \\ \dot{x}_{L_e} \end{Bmatrix}}_{\dot{x}_e} = \underbrace{\begin{bmatrix} 0 & I & 0 & 0 \\ A_{ee_0} & A_{ee_1} & A_{eL} & A_{eL} \\ 0 & E_{Le} & \frac{V}{c}R & 0 \\ 0 & E_{Le} & 0 & \frac{V}{c}R \end{bmatrix}}_{A} \underbrace{\begin{Bmatrix} \eta_e \\ \dot{\eta}_e \\ x_{L_{as}} \\ x_{L_e} \end{Bmatrix}}_{x_e} + \underbrace{\begin{bmatrix} 0 & 0 & 0 \\ B_{e_0} & B_{e_1} & B_{e_2} \\ 0 & 0.5E_{L\delta} & 0 \\ 0 & 0.5E_{L\delta} & 0 \end{bmatrix}}_{B_1} \underbrace{\begin{Bmatrix} \delta_u \\ \delta_{\dot{u}} \\ \delta_{\ddot{u}} \end{Bmatrix}}_{\delta_U} + \underbrace{\begin{bmatrix} 0 & 0 \\ A_{er_0} & A_{er_1} \\ E_{L*} & E_{Lr} \\ 0 & 0 \end{bmatrix}}_{B_2} \underbrace{\begin{Bmatrix} \delta_{\xi_{as}} \\ \delta_{\dot{\xi}_{as}} \end{Bmatrix}}_{\delta_\xi} + \underbrace{\begin{bmatrix} 0 & 0 \\ B_{ew1} & B_{ew2} \\ 0 & 0.5E_{rG} \\ 0 & 0.5E_{rG} \end{bmatrix}}_{B_3} \underbrace{\begin{Bmatrix} w_G \\ \dot{w}_G \end{Bmatrix}}_{w} \quad (38)$$

where $\delta_{\xi_{as}}$ and δ_u are defined as the incremental airframe states and inputs (perturbation from trim values):

$$\delta_{\xi_{as}} = \xi_{as} - \xi_{as|_0} \quad (39)$$

$$\delta_u = u - u_{|0} \quad (40)$$

$\xi_{as|_0}$ and $u_{|0}$ being the airframe state and input vectors computed at some specific trim condition ab initio of the simulation run. Using a short notation form, Eq. (38) can be expressed as

$$\dot{x}_e = Ax_e + B_1\delta_U + B_2\delta_\xi + B_3 w \quad (41)$$

The previous equation is used to estimate the elastic and lag states as a function of the incremental control input ($\delta_U^T = [\delta_u^T, \delta_{\dot{u}}^T, \delta_{\ddot{u}}^T]^T$) and incremental airframe states ($\delta_\xi^T = [\delta_{\xi_{as}}^T, \delta_{\dot{\xi}_{as}}^T]^T$) at each time iteration.

The quasi-static elastic deformation η_{e0} is computed by static residualization of the elastic modes; that is, the $\dot{\eta}_e = \ddot{\eta}_e = x_{Le} = 0$ condition needs to be fulfilled. Therefore, the quasi-static elastic influence is estimated from Eq. (41) as

$$\dot{x}_e = 0 \Rightarrow x_e = -A^{-1}(B_1\delta_U + B_2\delta_x i + B_3 w) \quad (42)$$

and from x_e, the quasi-static elastic influence vector η_{e0} can be recovered.

In summary, the linear aeroelastic solver will be built based on the following:

1. Apply algebraic Eq. (35) to compute the incremental aeroelastic loads Δ_F and Δ_M.

2. First-order differential Eq. (41) is used to compute the generalized coordinate-related vectors $\bar{\eta}_e$, $\dot{\eta}_e$, and $\ddot{\eta}_e$, as well as the aerodynamic lag terms related with the elastic modes, x_{L_e}.

3. Apply algebraic Eq. (42) to estimate the quasi-static deformation vector η_{e_0} at that specific flight condition.

Figure 7 illustrates the interconnection of the F/A-18 AAW 6-DOF dynamics subsystem, the incremental aeroelastic solver, the control surface mixer, and the control command transform blocks.

B. Closed Loop F/A-18 Active Aeroelastic Wing Linear Model with Gust Excitation

To demonstrate the proposed feedforward filter design algorithm, a simplified closed-loop F/A-18 AAW linear Simulink model with gust excitation is developed/implemented for the evaluation purposes. This high-fidelity aeroelastic model was developed using the following elements:

1) Six-DOF solver is generated using an Euler angles subsystem.

2) The generic flight control law is implemented.

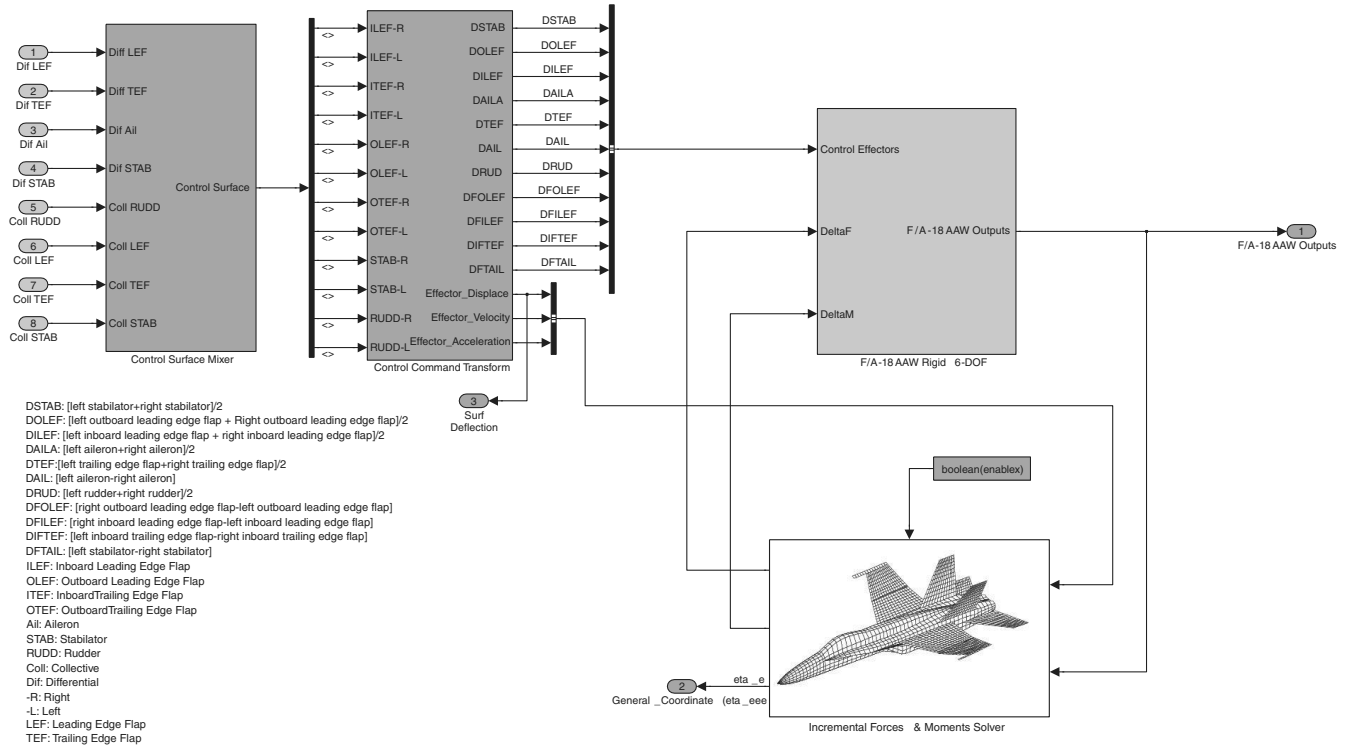

Fig. 7 Addition of the incremental aeroelastic loads solver to the nonlinear rigid-body 6-DOF subsystem.

3) Actuators and sensors are used.

4) Aerodynamic forces and moments subsystem is created, using the set of nondimensional stability and control derivatives obtained through a set of AAW PID flight tests.

5) An incremental aeroelastic load solver is built, including gust excitation generated by the ZAERO software system, using RFA techniques.

For continuous vertical gust perturbation, a low-pass filter followed by a Dryden vertical velocity shaping filter is used to shape the power of the gust perturbation. The low-pass filter is used to obtain the derivative of the gust perturbation. The low-pass filter is given as $T_{\mathrm{LPF}}(s) = \frac{a}{s+a}$, where $a = 200\pi$ rad/s is chosen in the remainder of the section.

The Dryden vertical velocity shaping filter is given as

$$T_g(s) = \sigma_{w_G} \frac{\sqrt{3}\tau_g^{-1/2} s + \tau_g^{-3/2}}{(s + 1/\tau_g)^2}$$

where $\tau_g = L_g/V$ ($L_g = 1750$ ft), and V is the aircraft body axis velocity; $\sigma_{w_G} = 100$ ft/s.

For a more detailed development of the F/A-18 AAW Simulink model with gust excitation, please refer to the NASA Small

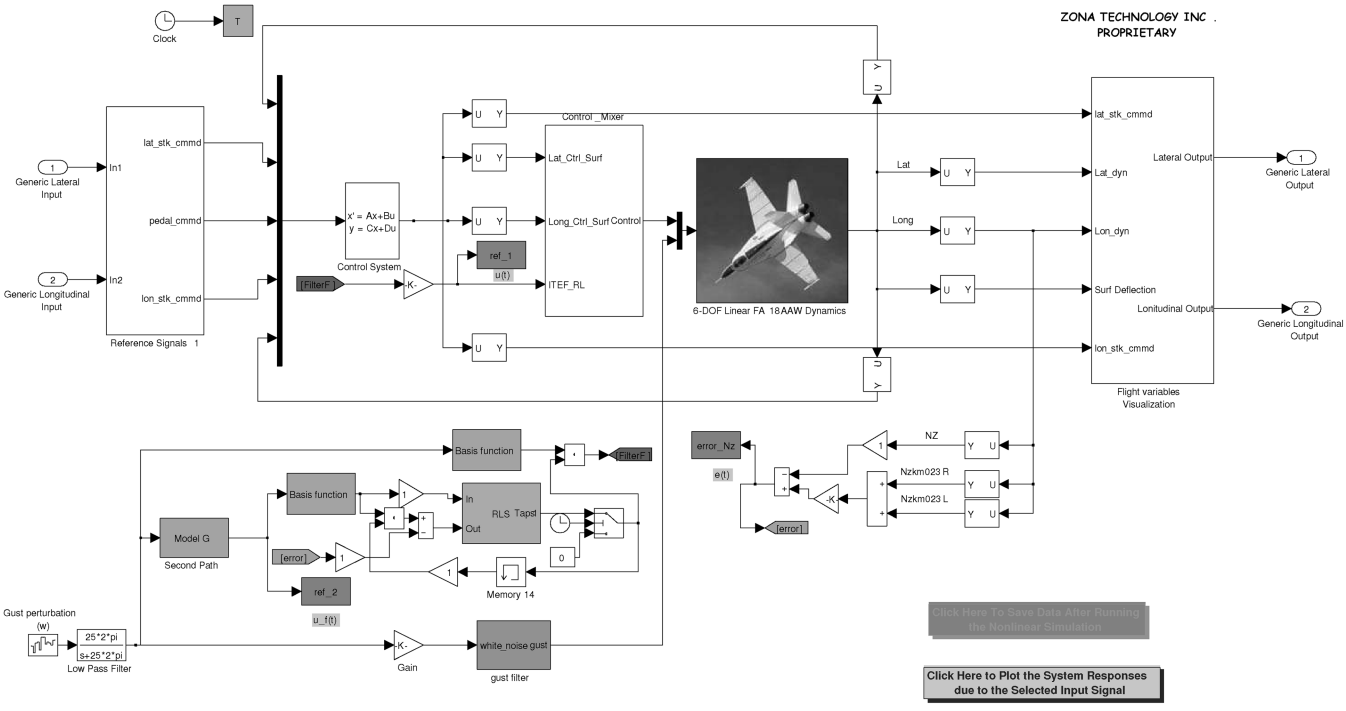

Fig. 8 Closed-loop F/A-18 AAW linear Simulink model.

Business Innovation Research (SBIR) Phase 1 final report [27]. The implementation of the adaptive feedforward control algorithm to the linearized F/A-18 AAW Simulink model is illustrated in Fig. 8. It should be noted that, during the simulation study considered in this paper, the dynamics of the airborne LIDAR turbulence sensor have not been considered. We assume that a perfect gust perturbation can be measured by the airborne LIDAR turbulence sensor (i.e., the sensor dynamics have an ideal constant dynamic of 1). However, the practical effects of the airborne LIDAR turbulence sensor on the performance of the feedforward controller have to be addressed in a future study.

C. Implementation of the Adaptive Feedforward Control

The construction of the feedforward controller can be separated into two steps: initialization and recursive estimation of the filter. In the initialization step, a secondary path transfer function $G(q)$ is estimated, which is done by performing an experiment using an external signal injected into the left and right trailing edge flaps as the excitation signal and the error signal $e(t)$ as the output signal. Because $\hat{G}(q)$ is only used for filtering purposes, a high-order model can be estimated to provide an accurate reconstruction of the filtered input $\hat{u}_f(t)$ via

$$\hat{u}_f(t) = \hat{G}(q)w(t) \tag{43}$$

as described in Eq. (4).

To facilitate the use of the ORTFIR filter, a set of modal parameters needs to be extracted to build the ORTFIR filter using the frequency domain Polymax identification methodology in Sec. IV. With $\hat{u}_f(t)$ given in Eq. (43), and $d(t) = H(q)w(t)$ in place, the modal parameters can be easily estimated using the Polymax method. With the signals $d(t)$ and $\hat{u}_f(t)$ and the basis function $B_i(q)$, a recursive minimization of the feedforward filter is done via the recursive least-squares minimization technique, described in Sec. V.

The error signal $e(t)$ can be selected as the vertical accelerometer reading at the aircraft left/right wing folder positions (i.e., Nz_{km023R} or Nz_{km023L}). An alternative choice could be

$$e(t) = \left[\frac{Nz_{km023R} + Nz_{km023L}}{2} - Nz_{cg}\right] \tag{44}$$

In this paper, Eq. (44) is served as a feedback signal for the feedforward filter design purpose. The advantage of choosing Eq. (44) is that the rigid-body dynamics can be partly removed, and the vertical wing bending is still observed.

Upon initialization of the feedforward controller, a 20th-order ORTFIR model $\hat{G}(q)$ was estimated in order to create the filtered signal $\hat{u}_f(t)$. The amplitude bode plot of the estimated $\hat{G}(q)$ is shown in Fig. 9.

The modes used to build the orthonormal basis $B_i(q)$ are extracted from the stabilization diagram in Fig. 10. From Fig. 10, five elastic modes can be extracted, and they are shown in Table 4.

For implementation purposes, only $L = 2$ parameters in the ORTFIR filter are estimated. With a 10th-order basis $B_i(q)$, this amounts to a 20th-order ORTFIR filter. To evaluate the performance of the proposed ORTFIR filter for feedforward compensation, a 20th-order FIR Filter is also designed to reduce the vertical wing vibration.

For a clear performance comparison between the FIR filter and the ORTFIR filter, the frequency response of the Nz_{km023R} and Nz_{km023L} using the FIR filter and the ORTFIR filter are plotted in Figs. 11 and 12, respectively. The solid line in Fig. 11a is the auto spectrum of the accelerometer measurement Nz_{km023R} without a feedforward controller integrated in the system; the dashed line in Fig. 11a indicates the auto spectrum of the accelerometer measurement Nz_{km023R} with the adaptive feedforward controller, using the FIR filter added in the system; the dotted line in Fig. 11 shows the auto spectrum of the accelerometer measurement Nz_{km023R} with the adaptive feedforward controller using the ORTFIR filter added in the system. Figure 11b is the zoomed in plot of Fig. 11a in the frequency range of [4 30] Hz. It is clearly seen that with the ORTFIR filter, a better magnitude reduction

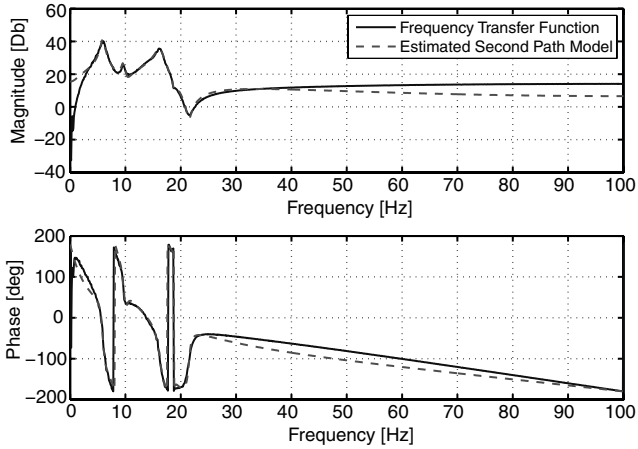

Fig. 9 Bode plot of the estimated 20th-order secondary path model $\hat{G}(q)$.

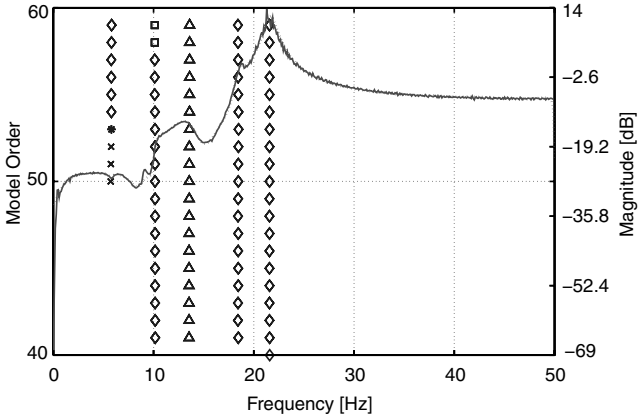

Fig. 10 Stabilization diagram.

of auto spectrum of Nz_{km023R} can be obtained in most of the frequency range compared with the FIR filter. Similar performance could also be observed in regard to Nz_{km023L}, which is shown in Figs. 12a and 12b.

The corresponding time responses are illustrated in Figs. 13 and 14. Figures 13b and 14b are the zoomed in plots of Figs. 13a and 14a, respectively. These time responses clearly demonstrate that, with the adaptive feedforward controller using an ORTFIR filter, a better structural vibration reduction can be obtained. From these figures, it is clearly demonstrated that both the FIR filter and the ORTFIR filter are efficient to reduce the normal acceleration at the left wing folder position and the right wing folder position. With the use of the both the ORTFIR filter and the FIR filter, the spectral content of the Nz_{km023R} and Nz_{km023L} have been reduced significantly in the frequency range from 2 to 20 Hz. However, with the use of the ORTFIR filter, more efficient vibration reduction performances are expected compared with the FIR filter.

Table 4 Estimated modes of feedforward filter using an FFT-based Polymax method

Mode number	Polymax identification	
	Frequency, Hz	Damping ζ, %
1	5.9246	4.5311
2	10.083	4.182
3	13.602	10.072
4	18.377	2.7409
5	21.569	2.5183

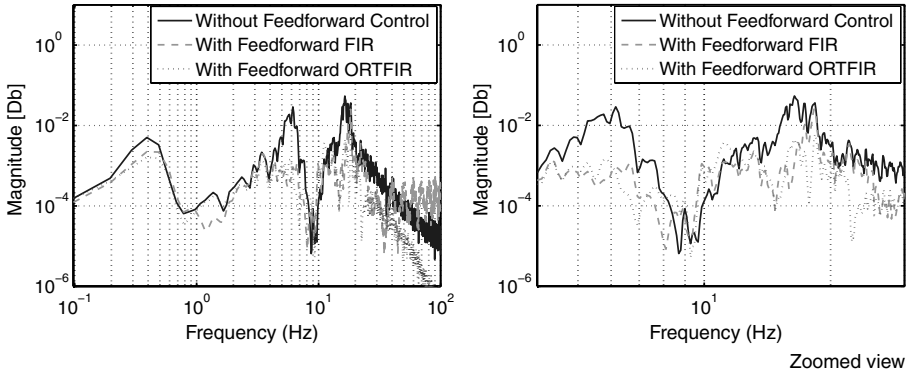

Fig. 11 Spectral content estimates of the Nz_{km023R} without control (solid), with control using the 20th-order FIR filter (dashed), and using the 20th-order ORTFIR Filter (dotted).

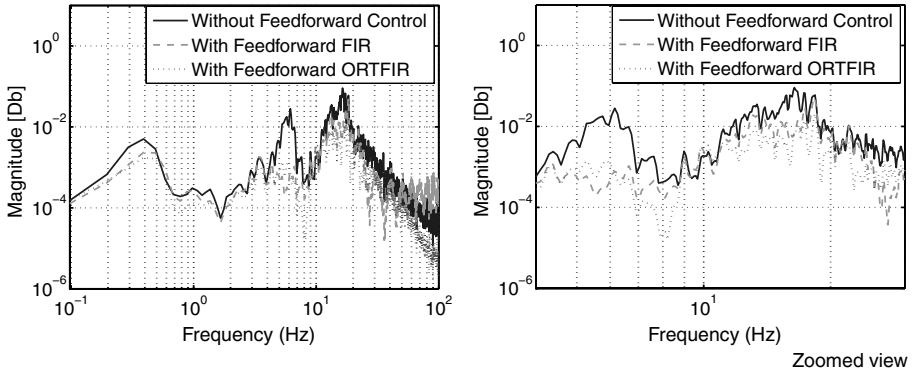

Fig. 12 Spectral content estimates of the Nz_{km023L} without control (solid), with control using the 20th-order FIR filter (dashed), and using the 20th-order ORTFIR filter (dotted).

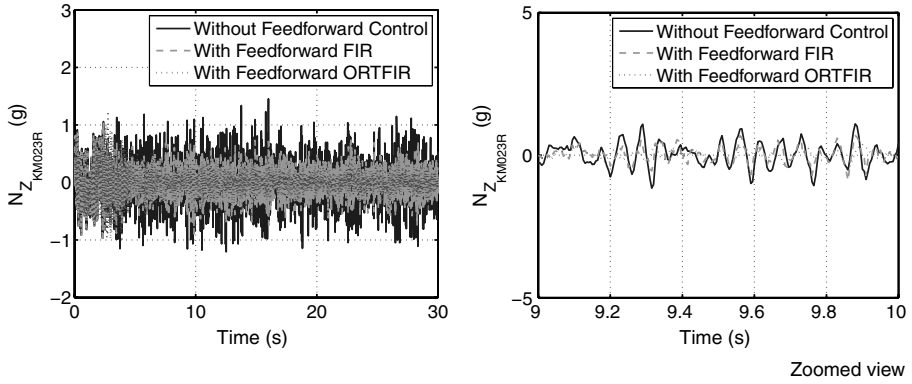

Fig. 13 Time domain response of the Nz_{km023R} without control (solid), with control using the 20th-order FIR filter (dashed), and using the 20th-order ORTFIR filter (dotted).

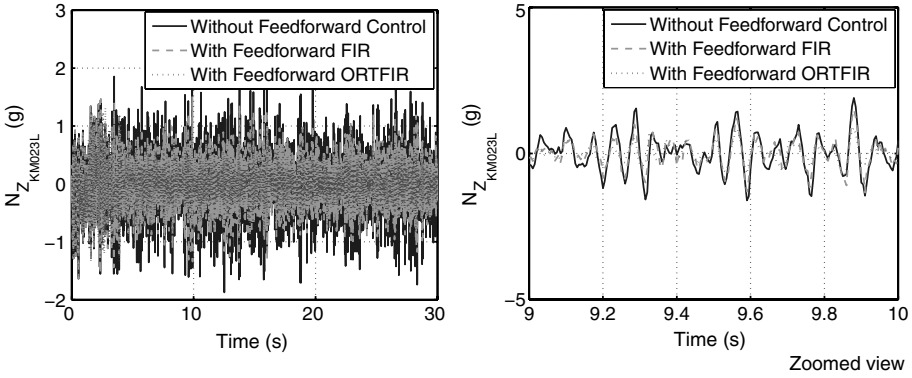

Fig. 14 Time domain response of the Nz_{km023L} without control (solid), with control using the 20th-order FIR filter (dashed), and with control using the 20th-order ORTFIR filter (dotted).

VII. Conclusions

In this paper, an adaptive feedforward control methodology has been proposed for the active control of gust load alleviation using an ORTFIR filter. The ORTFIR filter has the same linear parameter structure as a taped delay FIR filter, which is favorable for (recursive) estimation. The advantage of using the ORTFIR filter is that it allows the inclusion of prior knowledge of the flexible mode information of the aircraft dynamics in the parametrization of the filter for better accuracy of the feedforward filter.

In addition, by combing the flight dynamics model for rigid-body dynamics and an aeroelastic solver for aeroelastic incremental loads to accurately mimic inflight recorded dynamic behavior of the air vehicle, a unified integration framework that blends flight dynamics and the aeroelastic model is developed to facilitate the preflight simulation.

The proposed methodology in this paper is implemented on an F/A-18 AAW aeroelastic model developed with the unified integration framework. The feedforward filter is updated via the RLS technique with the variable forgetting factor at each time step. Compared with a traditional FIR filter and evaluated on the basis of the simulation data from the F/A-18 AAW aeroelastic model, it demonstrates that applying the adaptive feedforward controller using the ORTFIR filter yields a better performance of the gust loads alleviation of the aircraft.

Acknowledgments

Research is supported by NASA Dryden Flight Research Center under the SBIR Phase I contract NNX08CB12P. The authors would like to thank D. H. Baldelli, P. C. Chen and D. H. Lee for their support to build the F/A-18 AAW aeroelastic model.

References

[1] Schmidt, D., and Chen, T., "Frequency Domain Synthesis of a Robust Flutter Suppression Control Law," *Journal of Guidance, Control, and Dynamics*, Vol. 9, No. 3, 1986, pp. 346–351. doi:10.2514/3.20112

[2] Newsom, J. R., "Control Law Synthesis for Active Flutter Suppresion Using Optimal Control Theory," *Journal of Guidance, Control, and Dynamics*, Vol. 2, No. 5, 1979, pp. 388–394. doi:10.2514/3.55894

[3] Mahesh, J. K., Stone, C. R., Garrard, W. L., and Dunn, H. J., "Control Law Synthesis for Flutter Suppression Using Linear Quadratic Control Theory," *Journal of Guidance, Control, and Dynamics*, Vol. 4, No. 4, 1981, pp. 415–422. doi:10.2514/3.56094

[4] Garrard, W. L., and Liebst, B. S., "Active Flutter Suppression Using Eigenspace and Linear Quadratic Design Techniques," *Journal of Guidance, Control, and Dynamics*, Vol. 8, No. 3, 1985, pp. 304–311. doi:10.2514/3.19980

[5] Leibst, B. S., Garrard, W. L., and Farm, J. A., "Design of a Multivariable Fluter Suppression/Gust Load Alleviation System," *Journal of Guidance, Control, and Dynamics*, Vol. 11, No. 3, 1988, pp. 220–229. doi:10.2514/3.20297

[6] Woods-Vedeler, J. A., Pototzky, A., and Hoadley, S. T., "Rolling Maneuver Load Alleviation Using Active Controls," *Journal of Aircraft*, Vol. 32, No. 1, 1995, pp. 68–76. doi:10.2514/3.46685

[7] Barker, J. M., Balas, G. J., and Blue, P. A., "Active Flutter Suppression Via Gain-Scheduled Linear Fractional Control," *Proceedings of the American Control Conference*, IEEE, Piscataway, NJ, 1999, pp. 4014–4018.

[8] Eversman, W., and Roy, I. D., "Active Flutter Suppresion Using MIMO Adaptive LMS Control," 37th AIAA/ASME/ASCE/AHS/ASC Structures, Structural Dynamics, and Material Conference and Exhibit, AIAA Paper 1996-1345, 1996.

[9] Andrighettoni, M., and Mantegazza, P., "Multi-Input/Multi-Output Adaptive Active Flutter Suppression for a Wing Model," *Journal of Aircraft*, Vol. 35, No. 3, 1998, pp. 462–469. doi:10.2514/2.2319

[10] Wildschek, A., Maier, R., Hoffmann, F., Jeanneau, M., and Baier, H., "Active Wing Load Alleviation with an Adaptive Feedforward Control Algorithm," *AIAA Guidance, Navigation, and Control Conference and Exhibit*, AIAA Paper 2006-6054, 2006.

[11] Schmitt, N. P., Rehm, W., Pistner, T., Ziller, P., Diehl, H., and Navé, P., "The AWIATOR Airborne LIDAR Turbulence Sensor," *Aerospace Science and Technology*, Vol. 11, No. 7, 2007, pp. 546–552. doi:10.1016/j.ast.2007.03.006

[12] Baldelli, D. H., Zeng, J., Lind, R., and Harris, C., "Flutter-Prediction Tool for Flight-Test-Based Aeroelastic Parameter-VaryingModels," *Journal of Guidance, Control, and Dynamics*, Vol. 32, No. 1, 2009, pp. 158–171. doi:10.2514/1.36584

[13] Baldelli, D. H., and Zeng, J., "Unified Nonlinear Flight Dynamics Aeroelastic Solver Tool," NASA, TR NNL07AA85P, 2007.

[14] Schmitt, N., Rehm, W., Pistner, T., Diehl, H., Navé, P., Jenaro-Rabadan, G., Mirand, P., and Reymond, M., "Flight Test of the AWIATOR Airborne LIDAR Turbulence Sensor," *14th Coherent Laser Radar Conference*, Universities Space Research Assoc., Hunstville, AL, June 2007.

[15] Ljung, L., *System Identification: Theory for the User*, Prentice–Hall, Englewood Cliffs, NJ, 1999.

[16] Heuberger, P. S. C., Van Den Hof, P. M. J., and Bosgra, O. H., "A Generalized Orthonormal Basis for Linear Dynamical Systems," *IEEE Transactions on Automatic Control*, Vol. 40, No. 3, 1995, pp. 451–465. doi:10.1109/9.376057

[17] Ninness, B., and Gustafsson, F., "A Unifying Construction of Orthonormal Bases for System Identification," *IEEE Transactions on Automatic Control*, Vol. 42, No. 4, 1997, pp. 515–521. doi:10.1109/9.566661

[18] Zeng, J., and de Callafon, R. A., "Model Matching and Filter Design Using Orthonormal Basis Functions," *45th IEEE Conference on Decision and Control*, IEEE, Piscataway, NJ, 2006, pp. 5347–5352.

[19] Cauberghe, B., Guillaume, P., Verboven, P., Parloo, E., and Vanlanduit, S., "A Poly-Reference Implementation of the Maximum Likelihood Complex Frequency Domain Estimator and Some Industrial Applications," *Proceedings of the 22nd International Modal Analysis Conference*, SPIE, Bellingham, WA, Jan. 2004.

[20] Cauberghe, B., Guillaume, P., Verboven, P., Vanlanduit, S., and Parloo, E., "On the Influence of the Parameter Constraint on the Stability of the Poles and the Discrimination Capabilities of the Stabilisation Diagrams," *Mechanical Systems and Signal Processing*, Vol. 19, No. 5, 2005, pp. 989–1014.doi:10.1016/j.ymssp.2004.07.007

[21] Haykin, S., *Adaptive Filter Theory*, Prentice–Hall, Englewood Cliffs, NJ, 2002.

[22] Park, D. J., "Fast Tracking RLS Algorithm Using Novel Variable Forgetting Factor with Unity ZONE," *Electronics Letters*, Vol. 27, No. 23, 1991, pp. 2150–2151. doi:10.1049/el:19911331

[23] Baldelli, D. H., Chen, P. C., and Panza, J., "Unified Aeroelastic and Flight Dynamics Formulation Via Rational Function Approximations," *Journal of Aircraft*, Vol. 43, No. 3, 2006, pp. 763–772. doi:10.2514/1.16620

[24] Morelli, E. A., "Global Nonlinear Aerodynamic Modeling Using Multivariate Orthogonal Functions," *Journal of Aircraft*, Vol. 32, No. 2, 1995, pp. 270–277. doi:10.2514/3.46712

[25] Morelli, E. A., and Klein, V., "Accuracy of Aerodynamic Model Parameters Estimated from Flight Test Data," *Journal of Guidance, Control, and Dynamics*, Vol. 20, No. 1, 1997, pp. 74–80. doi:10.2514/2.3997

[26] Karpel, M., "Size Reduction Techniques for the Determination of Efficient Aeroservoelastic Models," *Control and Dynamic Systems: Advances in Theory and Applications*, Vol. 54, Academic Press, San Diego, CA, 1992, pp. 263–295.

[27] Zeng, J., and de Callafon, R. A., "Adaptive Feedforward/Feedback Control Framework," NASA TR NNX08CB12P, 2008.